Intracavity coherent supercontinuum generation via high-order soliton dynamics in a dissipative soliton fiber laser

YIWEI TIAN[1], FANCHAO MENG[1, 3], QI YAN[1], CHANGJIAN LV[1], ZHIXU JIA[1], WEIPING QIN[1], GUANSHI QIN[1, 4] AND JOHN M. DUDLEY[2, 5]

[1]*State Key Laboratory of Integrated Optoelectronics, College of Electronic Science and Engineering, Jilin University, Changchun 130012, China*
[2]*Institut FEMTO-ST, Université de Franche-Comté CNRS UMR 6174, Besançon, 25000, France*
[3]*fanchaomeng@jlu.edu.cn*
[4]*qings@jlu.edu.cn*
[5]*john.dudley@univ-fcomte.fr*

Abstract: High-order solitons exhibit fascinating dynamics during their propagation in anomalous dispersion media. High-order soliton dynamics have been intensively exploited for extreme pulse compression and coherent ultra-broadband spectrum generation. Despite recent advances, most previous studies have been restricted to soliton propagation external to a laser cavity, leaving the intracavity generation and evolution of high-order solitons less explored. Here we numerically demonstrate that by carefully optimizing the cavity parameters, intracavity coherent supercontinuum could be generated via high-order soliton dynamics in a dissipative soliton fiber laser. In particular, a positively chirped dissipative soliton is formed in normal dispersion gain fiber, which acts as a robust nonlinear attractor. After dechirping, a high (~8.5) order soliton was formed in a 1.1 m highly nonlinear fiber, which subsequently experienced significant intracavity temporal self-compression and spectral broadening. The shortest pulse duration was ~14 fs corresponding to ~2.7 optical cycles at 1551 nm, with the spectrum spanning over 600 nm at the -30 dB level. The generated supercontinuum maintains high coherence under quantum noise injection. In addition, the supercontinuum bandwidths were further optimized via a genetic algorithm, demonstrating the great promise of machine learning tools in optimizing complicated nonlinear systems. This work opens new possibilities for constructing compact and highly coherent supercontinuum light sources. Additionally, it provides valuable insights into the self-consistent evolution dynamics of high-order solitons within a fiber laser cavity.

1. Introduction

Supercontinuum light sources have found important applications in a variety of fields including optical frequency metrology [1], optical coherence tomography [2], bio-imaging [3], and sensing [4]. Despite the great success that has been achieved in supercontinuum generation by pumping a nonlinear medium outside a laser cavity [5-7], directly generating supercontinuum light from laser oscillators has arisen increasing research interest in recent years, because such systems have advantages in terms of stability, compactness, and cost. Furthermore, the supercontinuum generation process usually involves quite rich nonlinear dynamics. Exploring supercontinuum generation within a laser cavity, which naturally involves feedback, is crucial for advancing our understanding in nonlinear science.

By incorporating a highly nonlinear fiber (HNLF) into the laser cavity, supercontinuum was generated in fiber lasers that operated in the Q-switched operation regimes [8-11]. However, these Q-switched regimes often suffer from large pulse energy fluctuations. In contrast, intracavity supercontinuum has also been achieved in noise-like pulse (NLP) mode-locking regimes [12-14]. Recent real-time measurements using dispersive Fourier transform and time-lens techniques revealed that both the spectral and temporal profiles of such generated supercontinuum also exhibit fluctuations from roundtrip to roundtrip [15]. While incoherent supercontinuum generated from such systems has found important applications in tomography

and material processing [16-18], other applications such as precise frequency metrology [19] and coherent imaging [6] prefer a coherent supercontinuum with minimum fluctuations from shot to shot. However, generating highly coherent supercontinuum light directly from a mode-locked fiber oscillator remains a big challenge. The difficulty primarily stems from the excessive nonlinear phase accumulation required for supercontinuum generation, which complicates the self-consistent pulse evolution within the laser cavity. Recently, Ma et al. demonstrated an ultrabroad spectrum of ~400 nm (-20 dB level) directly output from a Mamyshev fiber oscillator with a HNLF [20]. In contrast to supercontinuum generated in the NLP regime, where the pulse envelope is incompressible [21] and typically with a duration of hundreds of ps [14,15], Ma et al. achieved a ~17 fs ultrashort pulse centered at ~1040 nm after dechirping the broadband pulse. Despite the significant bandwidth improvement achieved, they focused on supercontinuum generation only in the normal dispersion regime. Note that high-order soliton dynamics in anomalous dispersion fibers have been used in propagation experiments external to laser cavities for producing ultra-broadband spectra [5,22] and ultrashort temporal profiles [23,24]. However, although classic wave-packet structures such as average soliton [25-27] and similaritons [28-30] have been intensively investigated in fiber lasers, the question of whether high-order soliton could coherently evolve within each roundtrip in a laser cavity remains. Although some earlier studies in bulk oscillators have attributed unstable pulsation dynamics over multiple roundtrips to higher-order soliton effects [31,32], we focus here on fibre-laser systems where the circulating pulse precisely replicates its intensity profile after each roundtrip.

In particular, we propose a different approach for the intracavity coherent supercontinuum generation, where high-order soliton dynamics were exploited to achieve significant intracavity spectral broadening. A section of HNLF of anomalous dispersion is used, which facilitates high-order soliton evolution. We numerically demonstrate that a coherent supercontinuum spanning over 600 nm (at -30 dB level) with a pulse duration of ~14.1 fs (only 2.7 optical cycles) could be directly generated from a fiber oscillator. Furthermore, due to the complicated dynamics involved in such a highly nonlinear system with feedback, a genetic algorithm was employed to optimize the supercontinuum bandwidth.

2. Laser cavity configuration and Numerical model

2.1 Cavity configuration

The schematic of the fiber laser cavity is depicted in Fig. 1. The laser is a unidirectional ring cavity. We adopt a two-stage amplification in the cavity to provide a high enough gain for the pulse obtained after filtering the supercontinuum [33,34]. Although solutions could also be found with only a single piece of gain fiber, the two-stage amplification configuration typically makes finding a coherent supercontinuum solution easier. The parameters of the fibers are based on the realistic ones available in experiments. The pre-amplifier (EDF1, segment AB) consists of a 1.5 m Erbium highly doped fiber (LIEKKITM Er80-8/125) [27]. The main amplifier (EDF2, segment BC) consists of a 10.5 m Er-doped fiber (Nufern EDFC-980-HP) with normal dispersion which allows for a dissipative soliton to be developed [29,30]. A dispersion delay line (DDL) which can be constructed from bulk grating pairs or fiber Bragg gratings [20,35] was used to dechirp the pulse output from the gain fibers. The DDL significantly shortens the width and increases the peak power of the pulse [20]. A lumped loss, which includes both the splicing loss and the coupling loss, is implemented after the DDL with an equivalent transmittance ρ. A saturable absorber which can be realized with the nonlinear polarization rotation technique [15,27,29] ensures mode-locking. A 1.1 m HNLF (YOFC, NL1550-POS) of anomalous dispersion was used for intracavity supercontinuum generation. The splicing loss between the HNLF and an SMF pigtail is typically 0.75 dB per splicing, and it was equivalently considered in the transmittance ρ. To keep the model conceptually simple, output coupling is included as part of the lumped loss control parameter after the DDL, but it is straightforward to adapt the model to include output coupling at any particular point in the cavity. For example,

the generated supercontinuum can be easily coupled out after the HNLF with a coupler [15], and provided the coupling is relatively small (<10%) the same qualitative laser behavior is obtained with convergence to the same stable solution. A narrowband spectral filter controls the bandwidth of the pulse reinjected into the EDF1, which is crucial for the self-consistent evolution of the mode-locked pulse. Note that a filter is commonly used in dissipative soliton lasers [29,30,36,37], with this bandwidth control found to be critical to stabilize the pulse shaping and for self-consistent evolution after a round trip [36]. In particular, here the evolution of the pulse in the main amplifier (EDF2) is similar to a similariton with its spectrum notably broadened, and then the spectral bandwidth further dramatically increases in the HNLF due to high-order soliton dynamics. The spectral filtering is necessary since self-consistent oscillation requires bandwidth reduction before pulse reinjection into the amplifier. Note that we only consider key components in the cavity, leaving unnecessary fiber pigtails neglected to keep the model simple and clear. However, we have checked that similar results could still be obtained with a more realistic but cumbersome configuration that contains all fiber pigtails.

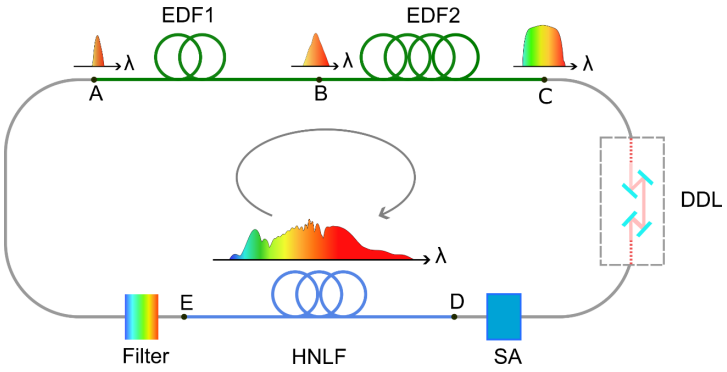

Fig. 1 Schematic of the laser cavity. EDF: erbium-doped fiber; DDL: dispersion delay line; HNLF: highly nonlinear fiber; SA: saturable absorber. Parameters for all cavity elements are given in the text.

2.2 Numerical model

The pulse propagation in each fiber segment is modeled by a modified scalar generalized nonlinear Schrödinger equation (GNLSE) [5,38,39]

$$\frac{\partial A}{\partial z}+\frac{i\beta_2}{2}\frac{\partial^2 A}{\partial \tau^2}-\frac{\beta_3}{6}\frac{\partial^3 A}{\partial \tau^3}-\frac{\hat{g}}{2}A=i\gamma\left(1+\frac{i}{\omega_0}\frac{\partial}{\partial \tau}\right)\left(A(z,\tau)\int_{-\infty}^{+\infty}R(t)|A(z,\tau-t)|^2\,dt\right), \quad (1)$$

where $A(z,\tau)$ denotes the complex envelope of the electric field, z is the propagation coordinate, τ is the co-moving time in the pulse frame, β_2 and β_3 are the second and third-order dispersion coefficients, γ is the nonlinearity parameter, $\omega_0=2\pi c/\lambda_0$ is the central angular frequency corresponding to 1550 nm. The nonlinear response function $R(t)=(1-f_R)\delta(t)+f_R h_R(t)$, where $f_R=0.18$ represents the fractional contribution of the Raman effect, and the Raman response function $h_R(t)=(\tau_1^{-2}+\tau_2^{-2})\tau_1\exp\left(-\frac{t}{\tau_2}\right)\sin(\frac{t}{\tau_1})$ with $\tau_1=12.2$ fs and $\tau_2=32$ fs [5,40]. The GNLSE is valid for a single-mode operation. Although strictly speaking the scalar GNLSE model is only ensured in a full-PM setup, it has been widely used to model the laser dynamics involving polarization evolution which usually results in good qualitive agreement with the experiment [20,29,30]. Note that although the mode field area dispersion effect may have impact on the achievable bandwidths [41], we have not included this higher-

order effect in our model. Nonetheless, the frequency-dependence which is present in the definition of the nonlinear coefficient γ which decreases the effective nonlinear strength for longer wavelengths has been included via the "self-steepening" term in the GNLSE. The parameters of the fibers are: $\beta_2^{(\mathrm{EDF1})} = -20 \times 10^{-3}$ ps^2/m, $\gamma^{(\mathrm{EDF1})} = 1.3 \times 10^{-3}$ W^{-1}m^{-1}, $\beta_2^{(\mathrm{EDF2})} = +20 \times 10^{-3}$ ps^2/m, $\gamma^{(\mathrm{EDF2})} = 3.3 \times 10^{-3}$ W^{-1}m^{-1}, $\beta_2^{(\mathrm{HNLF})} = -1.5 \times 10^{-3}$ ps^2/m, $\beta_3^{(\mathrm{HNLF})} = +30.1 \times 10^{-6}$ps^3/m, $\gamma^{(\mathrm{HNLF})} = 9.3 \times 10^{-3}$ W^{-1}m^{-1}, where third-order dispersion in the EDF is neglected [15]. The zero-dispersion wavelength (ZDW) of the HNLF is ~1489 nm. The gain term $\hat{g}_i(\omega)$ is non-zero only for the gain fibers and is modeled by [29,42],

$$\hat{g}_m(\Omega) = \frac{g_{0,m}}{1+E/E_{\mathrm{sat}}+\Omega^2/\Omega_g^2}, \tag{2}$$

where the index m = 1, 2 denote corresponding parameters for EDF1 and EDF2, respectively. $g_{0,1} = 2.3$ m^{-1} and $g_{0,2} = 0.55$ m^{-1} denote the small signal gains. $E = \int |A(\tau)|^2 d\tau$ denote the pulse energy, and $\Omega = \omega - \omega_0$ is the detuned angular frequency. The same gain bandwidth Ω_g (corresponds to 25 nm half-width) and gain saturation energy E_{sat} were used for both gain fibers. The DDL is modeled via an operator $\hat{D}_{\mathrm{DDL}}$, which is implemented in the frequency domain by $\hat{D}_{\mathrm{DDL}}\ \tilde{A}_{\mathrm{in}}(\Omega) = \tilde{A}_{\mathrm{in}}(\Omega)\exp(\frac{i}{2}D\Omega^2)$, where D= +0.2 ps^2 denotes the net dispersion provided by the DDL. The saturable absorber transmittance is modeled by the transfer function [29,39],

$$T(\tau) = 1 - \frac{q_0}{1+P(\tau)/P_{\mathrm{sat}}}, \tag{3}$$

where $q_0 = 0.9$ is the modulation depth, $P(\tau)$ is the instantaneous pulse power, and $P_{\mathrm{sat}} = 150$ W is the saturation power. In the simulation, the gain saturation energy E_{sat} which models the pump strength, the equivalent transmittance ρ after the DDL, the filter wavelength detuning $\delta\lambda_{0,F} = \lambda_{0,F} - \lambda_0$ (where $\lambda_{0,F}$ denotes the central wavelength of the filter), and the filter bandwidth $\Delta\lambda_{\mathrm{F}}$ are varied to find supercontinuum solutions in different cases as shown below. We used 2^{15} grid points with a 100 ps time window. The simulation of the laser was based on a standard piecewise roundtrip model [29,30,37]. Specifically, the initial field is iteratively propagated through each component within the cavity over many round trips until it converges to a steady state. To define a convergence of the laser, the relative error of the pulse energy ϵ between each two consecutive roundtrips is calculated. Then a convergence of the laser is considered to be satisfied if ϵ is below 10^{-6} for 300 roundtrips [43]. The simulations were initiated from the input to the EDF1 (point A) with a 300 fs Gaussian pulse with a peak power of 0.1 W to accelerate the convergence. Note that we have also checked a range of initial conditions, including a CW with random phase noise, and random intensity noise or a Gaussian pulse profile with random noise background. These different conditions can lead to the same high-order soliton solution with ultrabroad bandwidth, though for some noise seeds the laser can also converge to multiple-pulse state with much narrower bandwidth. It is because that multiple attractors could coexist in a highly nonlinear system [43]. Here we only focus on the ultra-broadband supercontinuum solution.

3. Results

3.1 Intracavity coherent supercontinuum generation via high-order soliton dynamics

The intracavity evolution of a typical solution is shown in Fig. 2. It was obtained with a parameter set {E_{sat} = 0.278 nJ, $\delta\lambda_{0,F} = 9.38$ nm, $\Delta\lambda_{\mathrm{F}} = 6.60$ nm, ρ = 0.260}. For the pulse energy convergence curve and the corresponding temporal and spectral evolution versus roundtrips, see Supplementary Fig. 1. The temporal and spectral evolutions versus the propagation distance over one cavity roundtrip are shown in Fig. 2(a), (b), respectively. The

labels A–E refer to the different points in the cavity shown in Fig. 1. The pulse was pre-amplified in EDF1 (segment AB) with anomalous dispersion and then amplified in EDF2 (segment BC) with normal dispersion. Notable variations can be observed in both the temporal pulse duration and the spectral bandwidth. The temporal and spectral profiles at points A, B and C are shown in Fig. 2(c). Panels (i)-(iii) in Fig. 2(c) presents the corresponding temporal intensity profiles and chirp of the pulse. The pulse duration (FWHM, full width at half maximum) decreases slightly in the EDF1, which are 0.64 ps and 0.59 ps at the input and output end of EDF1, respectively. The pulse is nearly unchirped at the input to the EDF1, while gains a slight positive chirp after output from EDF1 due to the self-phase modulation effect which overwhelms the negative chirp induced by the anomalous dispersion. While it broadens to 4.9 ps after output from EDF2 as shown in panel (iii) of Fig. 2(c), which exhibits a significant positive chirp induced by the large normal dispersion in EDF2. The pulse profile after the DDL was also shown in this panel, where the peak power increased over 11 times. The corresponding spectral profiles at points A, B and C are depicted in panel (iv) of Fig. 2(c). The spectral bandwidth in EDF1 has only a slight change, which remains ~5 nm. In contrast, the spectral bandwidth increases to 33 nm in EDF2 with a profile similar to the similariton [29]. Then after a lump loss after the DDL, the dechirped pulse was launched into the HNLF, where more dramatic evolutions happen for both the temporal and spectral profiles. The inset in Fig. 2(a) provides an expanded view of the temporal evolution within the HNLF (DE segment).

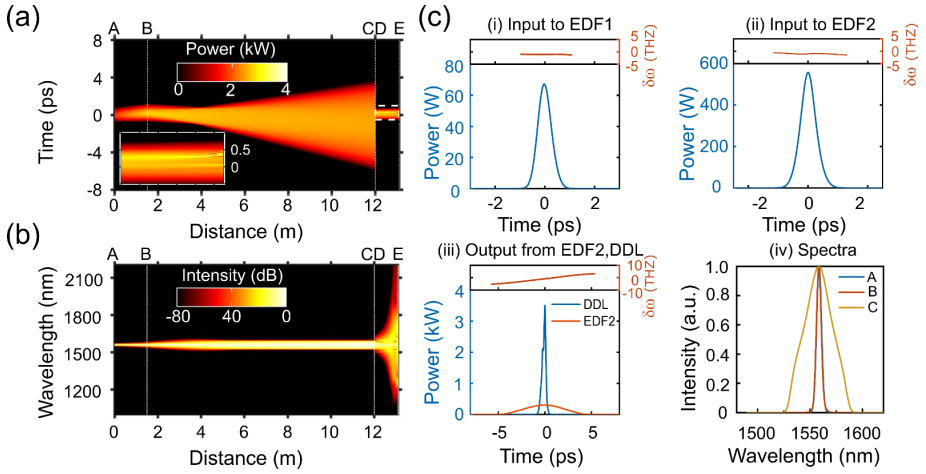

Fig.2 Typical intracavity pulse evolution. (a)Temporal evolution (linear color scale) along the cavity distance. The inset denotes an expanded view of the temporal evolution in the HNLF (DE segment). (b)The evolution of the spectrum on a logarithmic color scale. The labels A–E correspond to the cavity positions in Fig. 1. (c) The pulse chirp (right axis) and temporal intensity profiles (blue) at the (i) input to EDF1, (ii) input to EDF2, (iii) output from EDF2 and DDL. (iv) The corresponding spectrum at points A, B and C.

The spectral and temporal evolutions in the HNLF (segment DE in Fig. 2(a), (b)) are shown in Fig. 3(a), (b), respectively. Note the distance axis is offset such that the input end of the HNLF corresponds to the origin in Fig. 3. Clearly, high-order soliton dynamics dominate the spectral broadening process. The soliton order $N = \sqrt{\frac{\gamma P_0 T_0^2}{|\beta_2|}}$ of the input pulse was calculated to be ~8.4, where P_0 = 797 W, and T_0 = 120 fs was obtained from a $\sqrt{P_0}\mathrm{sech}(t/T_0)$ fitting of the main pulse. Since the nonlinear length $L_N = 1/\gamma P_0 =$ 0.135 m is much shorter than the dispersion length $L_D = T_0^2/|\beta_2| = 9.6$ m, the nonlinear effect dominates the initial propagation stage. Specifically, the self-phase modulation (SPM) effect gradually broadens the spectrum

from z = 0 m to z = 0.6 m in the HNLF. As the spectral bandwidth increases, the anomalous dispersion plays a more significant role which induces a negative chirp that compensates for the positive chirp caused by the SPM. This leads to a compression of the pulse duration and an increase in the peak power. As a result, the increased SPM effect further broadens the spectrum. Such a process continues during the pulse propagation, which eventually leads to a significant self-compression of the pulse after z = 0.9 m in the HNLF as shown in Fig. 3(b). The inset on the right of Fig. 3(b) represents a close-up view of the compressed pulse over a 200 fs time window. The maximum compression was reached at ~1.01 m in the HNLF with a peak power of 3871 W and a FWHM duration of 14.1fs. Notably, this corresponds to only ~2.7 optical cycles at its central wavelength (~1551 nm). The spectrogram [5,15] of the pulse at the maximum compression point is shown in Fig. 3(c). The corresponding temporal and spectral profiles are plotted on the top and right of the spectrogram, respectively. To obtain the spectrogram, we used an 80 fs Gaussian gate window. The spectrogram presents additional information on the transient frequency distribution along the complicated temporal profile. In particular, it can be identified that the dispersive wave centered at ~1267 nm is located around ~0.4 ps in the time window. In addition, the modulation in the spectrum around 1550 nm can also be explained by checking the spectrogram, where the same spectral components appear at different temporal locations, which leads to an interference in the spectrum. At the maximum compression point, the spectrum spans from 1224 nm to 1832 nm at -30 dB level, which extends over an octave (1125 nm to 2263 nm) at -60 dB level.

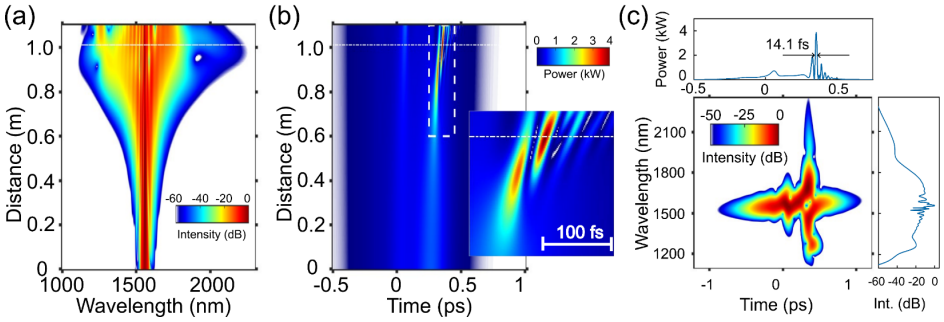

Fig. 3 Simulated pulse propagation dynamics in HNLF. (a) The evolution of the spectrum on a logarithmic scale. (b) Temporal evolution on a linear scale. An expanded view around the most compressed region (white dashed box) is shown on the right. The horizontal white dashed lines in (a, b) indicate the distance (~1.01 m) at which the shortest pulse duration is achieved. (c) The spectrogram of the shortest pulse at 1.01 m is shown on a logarithmic scale. The corresponding temporal profile and the spectrum are shown on the top and right, respectively.

To further investigate the coherence of the intracavity generated supercontinuum, we calculated the modulus of the complex degree of first-order coherence (DOC) $|g_{12}^{(1)}|$ which is defined by [5,44]

$$|g_{12}^{(1)}| = \left|\frac{<\tilde{E}_1^*(\lambda)\tilde{E}_2(\lambda)>}{\sqrt{<|\tilde{E}_1(\lambda)|^2><|\tilde{E}_2(\lambda)|^2>}}\right|, \quad (4)$$

where the angular brackets denote an ensemble average over independently generated pairs of spectra $\{\tilde{E}_1(\lambda), \tilde{E}_2(\lambda)\}$. Specifically, an ensemble of spectra was obtained by running 50 realizations. In each realization, different (one photon per mode) quantum noise was added into the laser pulse at the input to the gain fiber in each roundtrip, and the output spectrum from the HNLF was recorded after the laser reached a steady state (after 100 roundtrips). The ensemble of supercontinuum spectra obtained was then used for the calculation of the degree of first-order coherence. The results are shown in Fig. 4, where the top panels represent the temporal profiles

at three typical distances within the HNLF obtained from a particular simulation [44]. The pulse experienced significant self-compression at z = 0.8 m compared to that at z = 0.2 m, and it further splits into several ultrashort pulses at the output of the HNLF (z = 1.1 m) due to the perturbations such as the third-order dispersion and Raman effect. The bottom panels represent the calculated degree of first-order coherence (upper, right axis) and the spectral characteristics of the ensembles (lower, left axis) at corresponding distances. The average spectra are denoted by the solid red curves, while the grey dots denote the spectra of all the ensembles. In contrast to the broadband noise-like-pulse regimes [15,38], here the fluctuations of the shot-to-shot spectra are quite small, which yields a rather high degree of coherence (>0.9) over the broad spectral ranges.

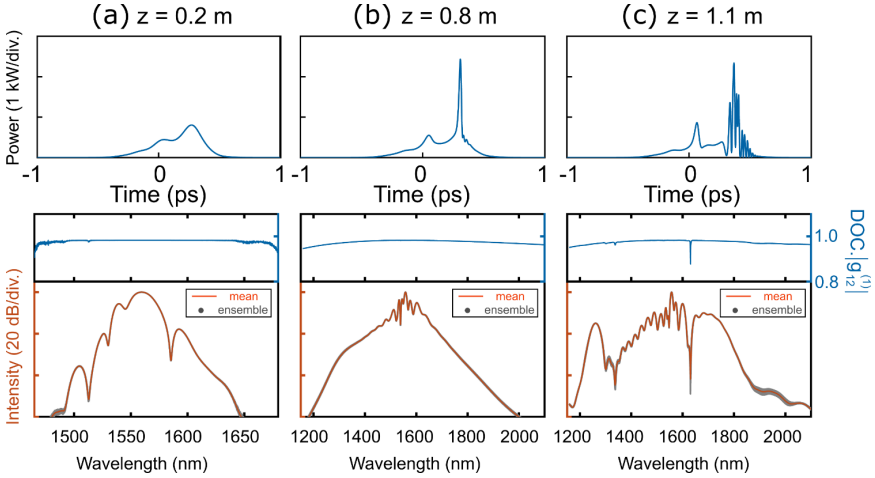

Fig. 4 Pulse profiles and coherence at propagation distances of (a) 0.2 m, (b) 0.8 m and (c) 1.1 m within the HNLF. The top panels represent temporal profiles obtained from a particular simulation. The upper blue curves in the bottom panels show the degree of coherence (right axis) for an ensemble of 50 realizations, and the lower red curves represent the mean spectra (left axis). Note that the ensemble spectra are also plotted together with the mean spectra with grey dots, although they are essentially indistinguishable because of the high degree of coherence.

3.2 Spectral bandwidth optimization with genetic algorithm

Although the high-order soliton dynamics yield ultra-broadband supercontinuum generation in a mode-locked fiber laser cavity, the feasible region in the parameter space is much narrower than that of a moderate-bandwidth mode-locking [39]. This makes it quite challenging to find supercontinuum mode-locking solutions. Recently, machine learning is showing great advantages for intelligent control and optimization in the field of ultrafast photonics [45-47]. Here we leverage the genetic algorithm (GA), which has emerged as a powerful workhorse for global multi-parameter optimizations in mode-locked lasers [48-51], for the optimization of the bandwidth of the coherent supercontinuum solution in the mode-locked fiber laser.

The schematic of the GA is shown in Fig. 5(a). The four-parameter set $\{E_{\mathrm{sat}}, \delta\lambda_{0,F}, \Delta\lambda_{\mathrm{F}}, \rho\}$ was used as genes of an "individual", which denote the gain saturation energy, the filter wavelength detuning, the filter bandwidth, and the equivalent transmittance after the DDL, respectively. We used standard genetic algorithm methods. Specifically, the algorithm starts with a population of 100 individuals with initial genes that are randomly selected. We select 5% as elite individuals that pass to the next generation unchanged, 70% for cross-over, and an adaptive mutation rate. The algorithm then optimizes the laser performance according to a compound fitness function, which includes the contributions from both the convergence of the

intracavity pulse iteration and the spectral bandwidth within the cavity. The fitness function F_{merit} is given by,

$$F_{\mathrm{merit}} = \xi_1 S_{\mathrm{conv}} + \xi_2 S_{\mathrm{BW}}, \tag{5}$$

where the first term on the r.h.s of Eq. (5) characterizes the convergence of the laser, with S_{conv} given by,

$$S_{\mathrm{conv}} = \epsilon_l \Theta(\epsilon_l - \epsilon_{\mathrm{TH}}) + \epsilon_{\mathrm{TH}} \Theta(\epsilon_{\mathrm{TH}} - \epsilon_l), \tag{6}$$

where $\epsilon_{\mathrm{TH}} = -5$ denotes a threshold characterizing the convergence of the iteration of the laser pulse, $\epsilon_l = \lg(\bar{\epsilon})$ with $\bar{\epsilon}$ denoting the mean of the relative error of the pulse energy between consecutive roundtrips, $\Theta(x)$ denotes the Heaviside step function. The second term on the r.h.s of Eq. (5) characterizes the intracavity spectral bandwidth with S_{BW} denoting the maximum spectral bandwidth (in nm) at the −50 dB level within the HNLF.

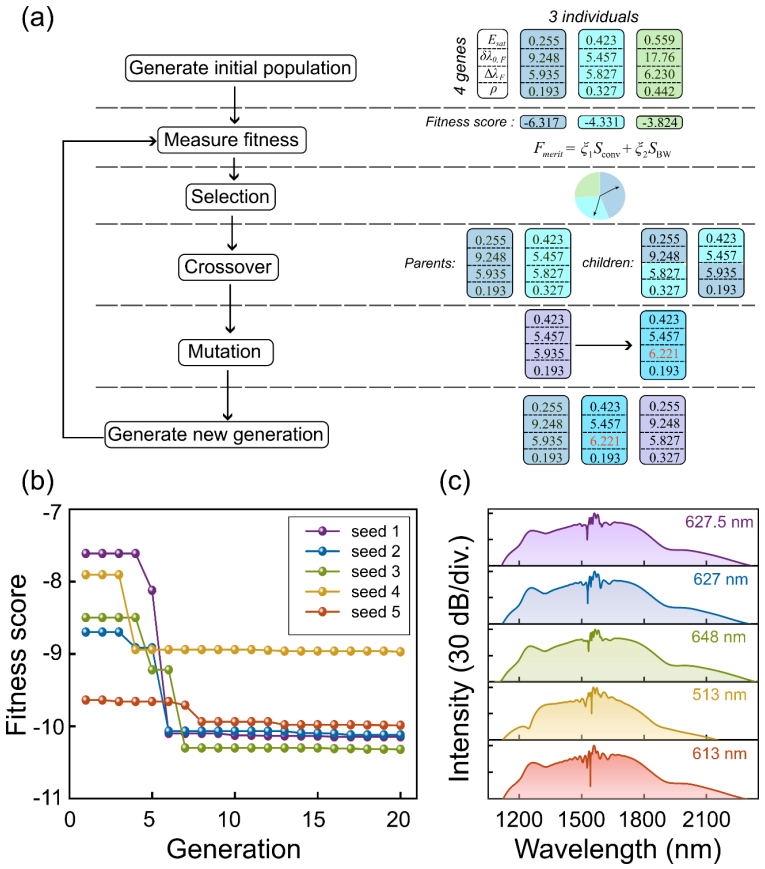

Fig. 5 (a) Schematic of the genetic algorithm. (b) Best score evolution with generations for five typical realizations initiated from different random seeds. (c) The best supercontinuum spectra generated in the HNLF found in each realization. Spectral bandwidths (at -30 dB) are indicated on the top right of each subplot.

The weight coefficients $\xi_1 = 1.0$ and $\xi_2 = -0.005$ in Eq. (5) denote the contributions of each term. Therefore, during the optimization, the first term in Eq. (5) guarantees obtaining a stable mode-locked solution, while the second term ensures obtaining a broadband solution. We have tested its performance over more than 20 runs. In practice, we found that a population of

100 individuals evolving over 20 generations typically was sufficient to give us coherent supercontinuum solutions. Within each generation, we iterated the laser pulse for 100 roundtrips for each individual.

Typical results from the GA optimization are shown in Fig. 5(b). To test the reliability of the GA, we performed multiple runs of the GA with different initial population seeds. The evolutions of the best score as a function of evolving generation obtained from five typical realizations are shown in Fig. 5(b). The optimum (broadest) spectrum obtained from each realization is shown in Fig. 5(c). The corresponding spectral widths at the -30 dB level are also indicated on the top right corner. Although the high dimension of parameter space, and the sensitivity to initial conditions of the highly nonlinear laser system, make searching a supercontinuum mode-locked solution extremely difficult, the GA was usually able to find solutions with bandwidth larger than 600 nm (at -30 dB).

4. Discussion and conclusion

Despite that great advances have been made in the coherent supercontinuum generations outside laser cavities, the realization of intracavity coherent ultra-broadband spectrum generation only emerges. The advantages of the latter approach are as follows. Firstly, the high circulating power within the laser cavity enables significantly more energy-efficient nonlinear spectral broadening compared to external laser systems designed to produce the same output power as an intracavity laser field. This makes laser supercontinuum sources highly suitable for applications requiring broad bandwidths but not necessarily high power, offering the added advantage of integration into compact experimental platforms. Secondly, supercontinuum generation dynamics constrained by the boundary conditions of a dissipative soliton laser cavity can ensure lower noise [20] better temporal coherence and stability, which is especially useful for applications requiring high coherence and stability across broad spectral ranges. Additionally, this approach could potentially enable the generation of carrier-envelope phase stabilized outputs at multiple wavelengths, paving the way for further applications in ultrafast optics and precision metrology. In contrast to the previous work [20] where the intracavity ultra-broadband spectrum was generated with normal dispersion, our approach leverages the high-order soliton dynamics in anomalous dispersion. By carefully optimizing the cavity parameters, stable mode-locked solution with coherent supercontinuum spectrum could be generated via high-order soliton dynamics in a dissipative soliton fiber laser.

It is useful to briefly discuss the stability condition of the mode-locked supercontinuum solution. Although four control parameters $\{E_{\mathrm{sat}}, \delta\lambda_{0,F}, \Delta\lambda_{\mathrm{F}}, \rho\}$ were used in finding stable solutions, we have chosen two parameters, i.e., $\{E_{\mathrm{sat}}, \rho\}$ to plot a stability map of a single-pulse operation, which is convenient for visualization (for details, see supplementary Fig. 2a). A full stability study over the whole four-dimensional parameter space would be an area of future study. A stable region was obtained when E_{sat} varies within the interval [0.270 nJ, 0.292 nJ] and ρ within the interval $[0.240, 0.275]$. Interestingly, bifurcation solutions were found near the stability boundary (see supplementary Fig. 2c, 2d). Moreover, we have also investigated the impact of the second-order dispersion (GVD), third-order dispersion (TOD) and the Raman fraction f_{R} on the stability of the solution. We studied the stability of the solution shown in Fig. 2 by scaling each one of the three parameters ($\beta_2^{(\mathrm{HNLF})}, \beta_3^{(\mathrm{HNLF})}, f_{\mathrm{R}}$) with the other two fixed. The stability maintained when the GVD and TOD were scaled within [0.81, 1.02] and [0.90, 3.69], respectively. The stability also maintained when the Raman fraction f_{R} was varied within [0.172, 0.282].

Although the high-order soliton propagations may be more susceptible to perturbations, leading to narrower feasible (solution) regions in the parameter space, machine learning tools such as GA exhibit great promise in finding such challenging solutions. It is even reasonable to anticipate an experimental realization of the high-order soliton laser by use of machine learning-based feedback algorithms [49,51,52] and a careful design of the HNLF dispersion and nonlinearity [53]. Furthermore, a more complete model that includes the mode area dispersion

effect [41], and the vector effect of the field [15] would be expected to be necessary in order to achieve full quantitative agreement with experiment. Moreover, we note that the noise model assumed in this work is a simplified approach, and more studies should be undertaken to investigate different noise sources, such as Gaussian noise within the EDFA bandwidth [54].

In conclusion, we have demonstrated numerically, for the first time, coherent supercontinuum generation in a fiber laser via high-order soliton dynamics. By carefully optimizing the parameters of the laser cavity, which incorporates a DDL and a HNLF of anomalous dispersion, intracavity coherent supercontinuum was generated. A minimum duration as short as 14.1 fs corresponding to 2.7 optical cycles at 1551 nm was obtained directly in the laser cavity. The intracavity temporal and spectral evolution highlights the critical role of the high-order soliton self-compression dynamics in the supercontinuum generation. In addition, an optimization of the laser performance was realized with a GA, where solutions with bandwidth typically larger than 600 nm (at -30 dB) were found. These results provide a new approach for constructing coherent supercontinuum light sources and may trigger further interest in applications of intracavity high-order soliton dynamics.

Funding. National Key Research and Development Program of China (2023YFB3611000); National Natural Science Foundation of China (62205121, 62235014, 62090063, 62075082, U20A20210, 61827821, U22A2085); the Opened Fund of the State Key Laboratory of Integrated Optoelectronics. Agence Nationale de la Recherche (OPTIMAL ANR-20-CE30-0004, EIPHI-BFC ANR-17-EURE-0002)

Disclosures. The authors declare no conflict of interest.

Data availability. Data underlying the results presented in this paper are not publicly available at this time but may be obtained from the authors upon reasonable request.

Supplementary Document. See Supplement 1 for supporting content.

References

1. T. Udem, R. Holzwarth, and T. W. Hänsch, "Optical frequency metrology," Nature **416**(6877), 233-237 (2002).
2. I. Hartl, X. Li, C. Chudoba, et al., "Ultrahigh-resolution optical coherence tomography using continuum generation in an air–silica microstructure optical fiber," Opt. Lett. **26**(9), 608-610 (2001).
3. E. Auksorius, B. R. Boruah, C. Dunsby, et al., "Stimulated emission depletion microscopy with a supercontinuum source and fluorescence lifetime imaging," Opt. Lett. **33**(2), 113-115 (2008).
4. C. Kaminski, R. Watt, A. Elder, et al., "Supercontinuum radiation for applications in chemical sensing and microscopy," Appl. Phys. B: Lasers Opt. **92**, 367-378 (2008).
5. J. M. Dudley, G. Genty, and S. Coen, "Supercontinuum generation in photonic crystal fiber," Rev. Mod. Phys. **78**(4), 1135-1184 (2006).
6. A. Rampur, D.-M. Spangenberg, B. Sierro, et al., "Perspective on the next generation of ultra-low noise fiber supercontinuum sources and their emerging applications in spectroscopy, imaging, and ultrafast photonics," Appl. Phys. Lett. **118**(24), 240504 (2021).
7. T. Sylvestre, E. Genier, A. N. Ghosh, et al., "Recent advances in supercontinuum generation in specialty optical fibers," J. Opt. Soc. Am. B **38**(12), F90-F103 (2021).
8. S. Chernikov, Y. Zhu, J. Taylor, et al., "Supercontinuum self-Q-switched ytterbium fiber laser," Opt. Lett. **22**(5), 298-300 (1997).
9. A. Roy, M. Laroche, P. Roy, et al., "Q-switched Yb-doped nonlinear microstructured fiber laser for the emission of broadband spectrum," Opt. Lett. **32**(22), 3299-3301 (2007).
10. J. Cascante-Vindas, A. Diez, J. Cruz, et al., "Supercontinuum Q-switched Yb fiber laser using an intracavity microstructured fiber," Opt. Lett. **34**(23), 3628-3630 (2009).
11. H. Cheng, Z. Luo, Y. Huang, et al., "Low-threshold supercontinuum generation and optimization of PCF-intracavity-excited Q-switched fiber lasers," Opt. Commun. **321**, 145-149 (2014).
12. L. A. Vazquez-Zuniga, and Y. Jeong, "Super-broadband noise-like pulse erbium-doped fiber ring laser with a highly nonlinear fiber for Raman gain enhancement," IEEE Photonics Technol. Lett. **24**(17), 1549-1551 (2012).
13. M. López-Ripa, S. Jarabo, and F. J. Salgado-Remacha, "Near-infrared supercontinuum source by intracavity silica-based highly-nonlinear fiber," Opt. Lett. **44**(8), 2016-2019 (2019).
14. X. Wang, A. Komarov, M. Klimczak, et al., "Generation of noise-like pulses with 203 nm 3-dB bandwidth," Opt. Express **27**(17), 24147-24153 (2019).
15. F. Meng, C. Lapre, C. Billet, et al., "Intracavity incoherent supercontinuum dynamics and rogue waves in a broadband dissipative soliton laser," Nat. Commun. **12**(1), 5567 (2021).

16. Y. Jeong, L. A. Vazquez-Zuniga, S. Lee, et al., "On the formation of noise-like pulses in fiber ring cavity configurations," Opt. Fiber Technol. **20**(6), 575-592 (2014).
17. S. Keren, and M. Horowitz, "Interrogation of fiber gratings by use of low-coherence spectral interferometry of noiselike pulses," Opt. Lett. **26**(6), 328-330 (2001).
18. K. Özgören, B. Öktem, S. Yilmaz, et al., "83 W, 3.1 MHz, square-shaped, 1 ns-pulsed all-fiber-integrated laser for micromachining," Opt. Express **19**(18), 17647-17652 (2011).
19. T. Fortier, and E. Baumann, "20 years of developments in optical frequency comb technology and applications," Commun. Phys. **2**(1), 153 (2019).
20. C. Ma, A. Khanolkar, Y. Zang, et al., "Ultrabroadband, few-cycle pulses directly from a Mamyshev fiber oscillator," Photonics Res. **8**(1), 65-69 (2020).
21. S. Smirnov, S. Kobtsev, S. Kukarin, et al., "Three key regimes of single pulse generation per round trip of all-normal-dispersion fiber lasers mode-locked with nonlinear polarization rotation," Opt. Express **20**(24), 27447-27453 (2012).
22. F. Meng, B. Liu, S. Wang, et al., "Controllable two-color dispersive wave generation in argon-filled hypocycloid-core kagome fiber," Opt. Express **25**(26), 32972-32984 (2017).
23. T. Balciunas, C. Fourcade-Dutin, G. Fan, et al., "A strong-field driver in the single-cycle regime based on self-compression in a kagome fibre," Nat. Commun. **6**(1), 6117 (2015).
24. E. A. Stepanov, A. A. Voronin, F. Meng, et al., "Multioctave supercontinua from shock-coupled soliton self-compression," Phys. Rev. A **99**(3), 033855 (2019).
25. S. Kelly, K. Smith, K. Blow, et al., "Average soliton dynamics of a high-gain erbium fiber laser," Opt. Lett. **16**(17), 1337-1339 (1991).
26. L. E. Nelson, D. Jones, K. Tamura, et al., "Ultrashort-pulse fiber ring lasers," Appl. Phys. B 65(2) (1997).
27. T. Zhang, F. Meng, Q. Yan, et al., "Significant enhancement of multiple resonant sidebands in a soliton fiber laser," Photonics Res. **11**(11), 1847-1860 (2023).
28. F. Ilday, J. Buckley, W. Clark, et al., "Self-similar evolution of parabolic pulses in a laser," Phys. Rev. Lett. **92**(21), 213902 (2004).
29. B. Oktem, C. Ülgüdür, and F. Ö. Ilday, "Soliton–similariton fibre laser," Nat. Photonics **4**(5), 307-311 (2010).
30. C. Lapre, C. Billet, F. Meng, et al., "Real-time characterization of spectral instabilities in a mode-locked fibre laser exhibiting soliton-similariton dynamics," Sci. Rep. **9**(1), 13950 (2019).
31. F. Salin, P. Grangier, G. Roger, et al., "Observation of high-order solitons directly produced by a femtosecond ring laser," Phys. Rev. Lett. **56**(11), 1132 (1986).
32. D. Reid, J. Dudley, M. Ebrahimzadeh, et al., "Soliton formation in a femtosecond optical parametric oscillator," Opt. Lett. **19**(11), 825-827 (1994).
33. J. Girardot, A. Coillet, M. Nafa, et al., "On-demand generation of soliton molecules through evolutionary algorithm optimization," Opt. Lett. **47**(1), 134-137 (2022).
34. P. M. Becker, A. A. Olsson, and J. R. Simpson, *Erbium-doped fiber amplifiers: fundamentals and technology* (Academic Press, 1999).
35. G. P. Agrawal, *Applications of nonlinear fiber optics*, 2nd ed. (Academic, 2008).
36. F. W. Wise, A. Chong, and W. H. Renninger, "High-energy femtosecond fiber lasers based on pulse propagation at normal dispersion," Laser Photonics Rev. **2**(1-2), 58-73 (2008).
37. R. I. Woodward, "Dispersion engineering of mode-locked fibre lasers," J. Opt. **20**(3), 033002 (2018).
38. M. Mabed, F. Meng, L. Salmela, et al., "Machine learning analysis of instabilities in noise-like pulse lasers," Opt. Express **30**(9), 15060-15072 (2022).
39. F. Meng, C. Lapre, C. Billet, et al., "Instabilities in a dissipative soliton-similariton laser using a scalar iterative map," Opt. Lett. **45**(5), 1232-1235 (2020).
40. G. Agrawal, *Nonlinear Fiber Optics* (Academic, 2013).
41. J. Laegsgaard, "Mode profile dispersion in the generalized nonlinear Schrödinger equation," Opt. Express **15**(24), 16110-16123 (2007).
42. P. W. Milonni, and J. H. Eberly, *Laser physics* (John Wiley & Sons, 2010).
43. T. Schreiber, B. Ortaç, J. Limpert, et al., "On the study of pulse evolution in ultra-short pulse mode-locked fiber lasers by numerical simulations," Opt. Express **15**(13), 8252-8262 (2007).
44. J. M. Dudley, and S. Coen, "Coherence properties of supercontinuum spectra generated in photonic crystal and tapered optical fibers," Opt. Lett. **27**(13), 1180-1182 (2002).
45. M. Jiang, H. Wu, Y. An, et al., "Fiber laser development enabled by machine learning: review and prospect," PhotoniX **3**(1), 16 (2022).
46. G. Genty, L. Salmela, J. M. Dudley, et al., "Machine learning and applications in ultrafast photonics," Nat. Photonics **15**(2), 91-101 (2021).
47. P. Freire, E. Manuylovich, J. E. Prilepsky, et al., "Artificial neural networks for photonic applications—from algorithms to implementation: tutorial," Adv. Opt. Photonics **15**(3), 739-834 (2023).
48. U. Andral, R. S. Fodil, F. Amrani, et al., "Fiber laser mode locked through an evolutionary algorithm," Optica **2**(4), 275-278 (2015).
49. R. Woodward, and E. J. Kelleher, "Towards 'smart lasers': self-optimisation of an ultrafast pulse source using a genetic algorithm," Sci. Rep. **6**(1), 37616 (2016).
50. C. Lapre, F. Meng, M. Hary, et al., "Genetic algorithm optimization of broadband operation in a noise-like pulse fiber laser," Sci. Rep. **13**(1), 1865 (2023).

51. Q. Yan, Y. Tian, T. Zhang, et al., "Machine learning based automatic mode-locking of a dual-wavelength soliton fiber laser," Photonics **11**(1), 47 (2024).
52. T. Baumeister, S. L. Brunton, and J. Nathan Kutz, "Deep learning and model predictive control for self-tuning mode-locked lasers," J. Opt. Soc. Am. B **35**(3), 617-626 (2018).
53. C. Yao, Z. Jia, Z. Li, et al., "High-power mid-infrared supercontinuum laser source using fluorotellurite fiber," Optica **5**(10), 1264-1270 (2018).
54. M. H. Frosz, "Validation of input-noise model for simulations of supercontinuum generation and rogue waves," Opt. Express **18**(14), 14778-14787 (2010).

Intracavity coherent supercontinuum generation via high-order soliton dynamics in a dissipative soliton fiber laser: supplemental document

1. Implementation of the iterative map model for the laser

The approach that we use to model the laser dynamics is the standard method for lasers operating as "dissipative soliton" systems where nonlinear and dispersive effects are present at the same time as gain, loss, spectral filtering and saturable absorption. Simulations using this approach have been performed for many years, and excellent reviews of the methodology appear in. Ref [1-3].

To model the laser dynamics, we use the standard iterative map model (piecewise roundtrip model) [2,4]. The basic idea is to begin with an initial complex-valued field profile (e.g. a low amplitude background noise field, or a noisy Gaussian pulse) and propagate this field numerically through each element of the laser cavity, modifying its temporal and spectral properties through dispersive and nonlinear propagation, and modifying its pulse energy through gain and loss. Gain can be simulated in different ways, but a widely used method is to use a Lorentzian based model including gain saturation [2,4,5]. After one roundtrip through all the elements, the complex field is reinjected into the cavity and the process iterates. This approach allows the energy to dynamically evolve at the same time as the pulse properties are being modified by other elements. The energy is modified from roundtrip to roundtrip, but the effect of gain saturation is associated with convergence to a constant energy state, and usually an invariant pulse shape. We note, however, that such a model has also been shown to allow modelling of many instability regimes of dissipative soliton lasers, including soliton oscillations [4,6] and noise-like pulse behaviour [4,7].

While this approach to laser modelling might be considered a "conceptual" or "toy" model because of its relative simplicity, it has nonetheless been shown to reproduce observed experimental behaviour under a wide range of conditions. Moreover, whilst exact quantitative agreement with experiment may not be expected (primarily because of the simplified gain model used) the model still yields predictions for pulse energy and duration etc that are comparable to measurements.

The convergence of the laser model can be defined in a variety of ways, however the relative error of the pulse energy between each two consecutive roundtrips (ϵ) is commonly used. Specifically, the pulse energy in roundtrip m is denoted as $E_{\mathrm{p}}(m)$, and the corresponding relative error of the pulse energy is given by $\epsilon(m) = \frac{|E_{\mathrm{p}}(m) - E_{\mathrm{p}}(m-1)|}{E_{\mathrm{p}}(m)}$. Then the convergence of the laser can be considered achieved if ϵ is below a threshold (typically 10^{-4} to 10^{-6}) for a certain number (300) of roundtrips.

The convergence evolution of the supercontinuum solution in Fig. 2 in the main manuscript is shown in Fig. S1. The iterations were initiated from the input to the EDF1 (point A) in Fig. 1 in the main manuscript with a 300 fs Gaussian pulse with a peak power of 0.1 W. Here the field after the HNLF is monitored. The evolution of the relative error of the pulse energy ϵ over 1000 roundtrips are plotted in Fig. S1(a). The laser starts to converge after ~70 roundtrips with $\epsilon < 10^{-6}$. The corresponding temporal and spectral evolution over 1000 roundtrips are shown in Fig. S1(b) and Fig. S1(c), respectively.

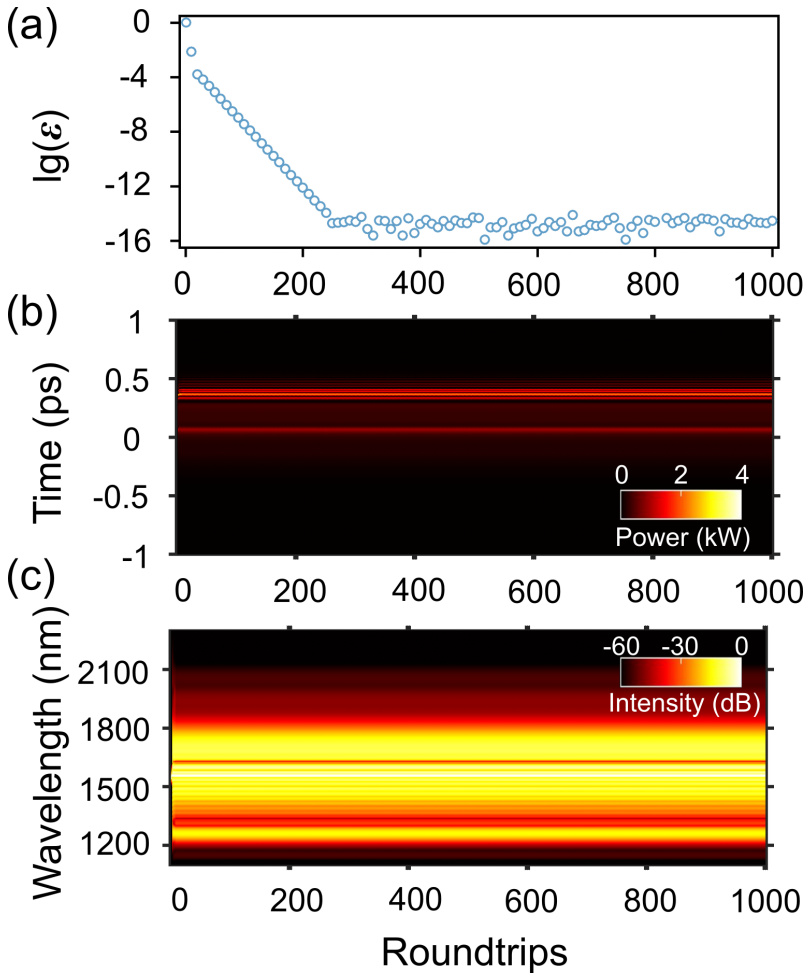

Fig. S1 (a) Logarithm of the relative error of the pulse energy versus the roundtrip number. (b) Temporal and (c) spectral evolution of the field after the HNLF over 1000 roundtrips.

2. Stability map of the mode-locked single-pulse supercontinuum operation

In order to explore the stability boundary of the mode-locked supercontinuum solution, two of the system parameters, i.e., the gain saturation energy E_{sat} and the equivalent transmittance after the DDL ρ were scanned. The stability (convergence) map is shown in Fig. S2(a), where the logarithmic mean error of the pulse energy $\lg(\bar{\epsilon})$ is plotted as a function of E_{sat} and ρ. The stable region corresponds to that shown in blue. We select six representative points (P1-P6) and the corresponding steady-state spectra are shown in Fig. S2(b). An unstable solution near the stability boundary is indicated by P7 in Fig. S2(a). It corresponds to a period-doubling bifurcation solution. The convergence curve over 200 roundtrips at P7 is shown in Fig. S2(c), and the inset presents the spectra after the HNLF for two consecutive roundtrips. The corresponding temporal and spectral evolutions are shown in Fig. S2(d), (e) respectively.

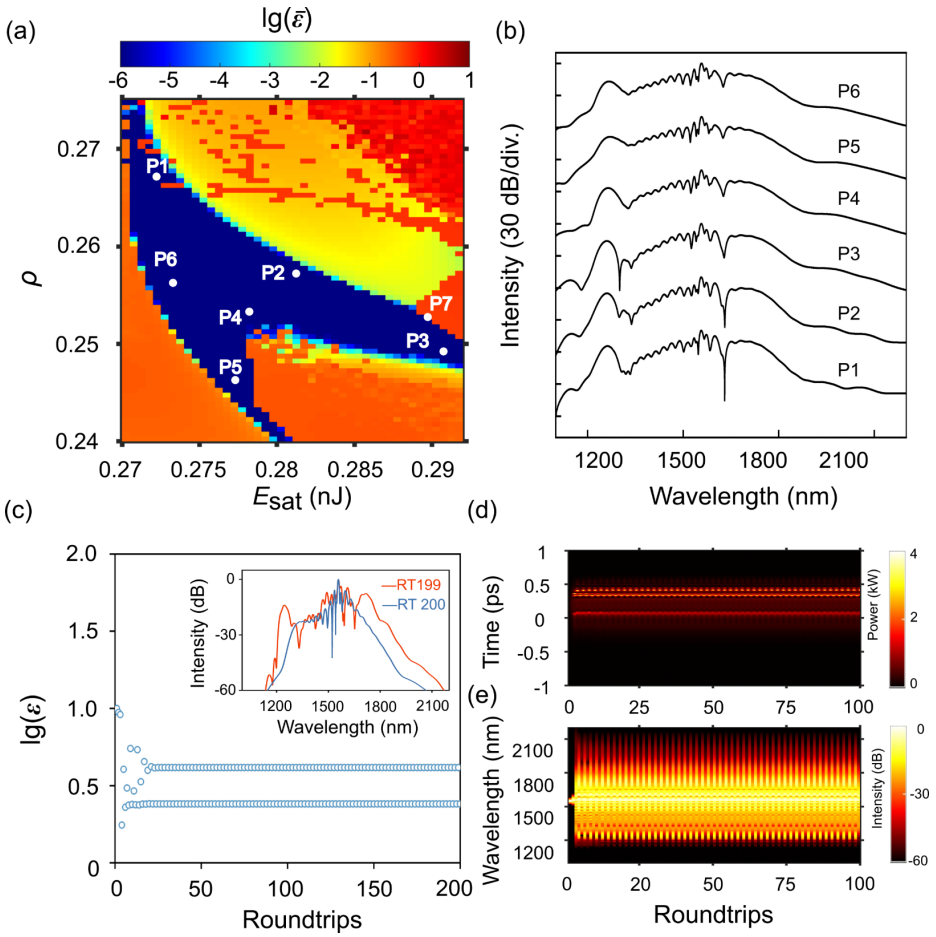

Fig. S2 (a) The stability (convergence) map as a function of the parameters Esat and ρ with $\delta\lambda_{0,F} = 9.38$ nm, $\Delta\lambda_F = 6.60$ nm. The parameters for P1-P6 are P1: {Esat = 0.272 nJ, ρ = 0.267}; P2: {Esat = 0.281 nJ, ρ = 0.257}; P3: {Esat = 0.291 nJ, ρ = 0.249}; P4: {Esat = 0.278 nJ, ρ = 0.253}; P5: {Esat = 0.277 nJ, ρ = 0.246}; and P6: {Esat = 0.273 nJ, ρ = 0.256}. (b) Output spectra at P1-P6. (c) Convergence curve at P7 with {Esat = 0.290 nJ, ρ = 0.252}. The inset denotes the spectra at two consecutive roundtrips (RT199 and RT200). (d) Temporal and (e) spectral evolution of the field after the HNLF over 1000 roundtrips at the parameter point P7.

References

S1. B. Oktem, C. Ülgüdür, and F. Ö. Ilday, "Soliton–similariton fibre laser," Nat. Photonics 4(5), 307-311 (2010).

S2. R. I. Woodward, "Dispersion engineering of mode-locked fibre lasers," J. Opt. **20**(3), 033002 (2018).

S3. S. K. Turitsyn, B. G. Bale, and M. P. Fedoruk, "Dispersion-managed solitons in fibre systems and lasers," Phys. Rep. **521**(4), 135-203 (2012).

S4. F. Meng, C. Lapre, C. Billet, et al., "Instabilities in a dissipative soliton-similariton laser using a scalar iterative map," Opt. Lett. **45**(5), 1232-1235 (2020).

S5. I. A. Yarutkina, O. V. Shtyrina, M. P. Fedoruk, et al., "Numerical modeling of fiber lasers with long and ultra-long ring cavity," Opt. Express **21**(10), 12942-12950 (2013).

S6. C. Lapre, C. Billet, F. Meng, et al., "Real-time characterization of spectral instabilities in a mode-locked fibre laser exhibiting soliton-similariton dynamics," Sci. Rep. **9**(1), 13950 (2019).

S7. Y. Jeong, L. A. Vazquez-Zuniga, S. Lee, et al., "On the formation of noise-like pulses in fiber ring cavity configurations," Opt. Fiber Technol. **20**(6), 575-592 (2014).